Contents lists available at ScienceDirect

Materials Today Bio

MnO2@Au nanostructures supported colorimetric biosensing with duplex-specific nuclease-assisted DNA structural transition

Xiaoyi Ma [a,b], Wuping Zhou [b], Haiwen Li [b], Bo Zhang [d,**], Peng Miao [a,b,c,*]

[a] University of Science and Technology of China, Hefei 230026, China
[b] Suzhou Institute of Biomedical Engineering and Technology, Chinese Academy of Sciences, Suzhou 215163, China
[c] Jinan Guokeyigong Science and Technology Development Co., Ltd., Jinan 250103, China
[d] Department of Radiology, The Second Affiliated Hospital of Soochow University, Suzhou 215004, China

ABSTRACT

Manganese dioxide (MnO_2) nanosheets are regarded as a new class of two-dimensional nanomaterials with several attractive properties with enormous progress in biomedical fields. Gold nanoparticles (AuNPs) are also important biocompatible nanomaterials with unusual optical properties. Hetero-nanostructure of MnO_2 and AuNPs with the medium of DNA is an interesting topic. In this work, the protection of the hetero-nanostructure from salt-induced aggregation is systematically investigated including the effects of sequence length, reagents concentrations, incubation time and temperature. The MnO_2@Au nanostructures are thus applied for the analysis of miRNA. Duplex-specific nuclease (DSN) catalyzed digestion, hybridization chain reaction (HCR) and catalytic hairpin assembly (CHA) are utilized for signal amplification. By finally analyzing the optical responses of the nanocomponents, highly sensitive analysis of target miRNA can be achieved. Excellent analytical performances are attributed to the unique features of MnO_2@Au nanostructures and signal amplification designs. They are promising basis for the construction of novel biosensors for clinical applications.

1. Introduction

Manganese dioxide (MnO_2) nanomaterials have attracted considerable attention due to their distinct electric, catalytic, ion-exchange, and optical properties [1–3]. MnO_2 possesses abundant surface hydroxyl groups and variable manganese valence states, which facilitate its high catalytic activity [4,5]. It also exhibits excellent extinction spectra from ultraviolet to far-infrared light, which can not only be applied in the utilization of solar energy and supercapacitors [6], but also show great application perspective for biomedical investigations [7–9]. For example, the photothermal conversion property endow MnO_2 good candidate for targeted cancer therapy [10]. Exceptionally larger surface area to mass ratio promises the high cargo-loading capacity for efficient drug delivery [11]. MnO_2 shows enzyme-like reaction profiles and substrate specificities, which can be applied as effective nanozymes for biosensing and therapy purposes [12–14]. There are various forms of MnO_2 structures including nanofibers [15], nanosheets [16], nanoparticles [17,18] and so on. Two-dimensional nanosheets have been found to possess many unusual properties with good flexibility [19–21]. MnO_2 nanosheets are

stacked with edge-sharing "MnO_6" octahedra with interlayer alkali ions [22]. The layered structures are robust with higher chemical and thermal stability compared with natural species [23].

The photophysical and photochemical properties of MnO_2 nanosheets (e.g., absorption capability with excellent molar extinction coefficient and effective fluorescence quenching or energy accepting capability) have led to various optical sensing or imaging applications [24]. However, there are only a few studies reported to explore the interactions between MnO_2 and biomacromolecules like DNA, which show excellent programming and self-assembly capabilities [25,26]. Our group previously optimized the length of single-stranded DNA, which can be adsorbed on the nanosheets with better affinity [27]. Since DNA can be easily conjugated with other nanomaterials, the nanosystem integrating multiple nanomaterials with the medium of DNA strands may exhibit great promise to develop into intelligent devices with outstanding performances [28–30]. It is highly desired to further understand the interaction between DNA modified MnO_2 nanosheets and other nanomaterials. Gold nanoparticles (AuNPs) have been extensively investigated due to their unique physical properties, which have been

---

used in the applications like catalyst, biosensor, bioimaging, photo-thermal therapy and so on [31–33]. Attaching DNA on the surface of AuNPs is one critical way for the functionalization, which has been intensively studied [34]. Successful modification requires the conservation of colloidal stability of the AuNPs system. Salt-aging method is commonly used because salt with high concentrations can effectively screen the charge repulsion between negatively charged DNA and AuNPs [35]. In recent years, more approaches have been developed including freezing method, pH-adjusting method and surfactant-assisted modification [36,37]. Freezing-driven DNA attachment shows certain merits. Especially, it does not rely on salt with heavy concentration and the attachment is quite fast. Cross-linking of two AuNPs can also be effectively avoided.

miRNAs play critical roles in a number of biological processes [38]. Abnormal expression of certain miRNAs are found to be associated with many diseases including cancers [39]. However, the features of low abundance, short length and high similarities of miRNA pose challenges of highly sensitive and selective analysis for early diagnosis purposes. Although traditional methods like reverse transcription polymerase chain reaction (RT-PCR) and microarray have been applied for miRNA assay with success, certain limits still exist including cumbersome steps of RT-PCR and insufficient sensitivity of microarray [40,41]. In order to address these issues, we have taken good use $MnO_2@Au$ nanostructures coupled with signal amplification designs. Smart DNA structural transitions are engineered by the use of duplex-specific nuclease (DSN) and certain strand displacement reactions, which attribute to the high signal amplification efficiency [42,43]. Two colorimetric biosensing strategies are developed. The characterizations show desirable analytical capabilities including high sensitivity, selectivity and rapid response. The developed nanosystem may also inspire further applications with the hybrid nanoplatform.

2. Experimental

2.1. Materials and instruments

Chloroauric acid ($HAuCl_4$) was from Shanghai Jiushan Chemicals Co., Ltd. (Shanghai, China). Trisodium citrate, tris (2-carboxyethly) phosphine (TCEP), ethylenediamineteraacetic acid (EDTA), manganese chloride ($MnCl_2$), ascorbic acid (AA), tetramethylammoniam hydroxide and hydrongen peroxide (H_2O_2) were purchased from Sigma (USA). DSN was ordered from Genomax Technologies Pte Ltd. (Singapore). Human serum samples were collected from local hospital with written consent from participants (Suzhou, China). All other chemicals were of analytical grade and used without further purification. All solutions used in this work were prepared with ultrapure water purified by a Millipore water purification system (specific resistance: 18 MΩ cm). All sequence were synthesized and purified by Sangon Biotechnology Co. Ltd. (Shanghai, China). UV–vis absorption spectra were measured by a Synergy HT multifunction microplate reader (BioTek Instruments,Inc., USA). Transmission electron microscopic (TEM) images were taken with a FEI Tecnai G20 transmission electron microscopy (FEI, USA).

2.2. Preparation of DNA modified AuNPs and MnO_2 nanosheets

Bare AuNPs were prepared by a citrate reduction method according to a previous report [44]. To achieve DNA modification, thiolated DNA strands were previously heated to 95 °C for 5 min and cooled to room temperature gradually. After that, 3 μM DNA was mixed with AuNPs, which was placed in a refrigerator freezer (−20 °C) for 2 h, followed by thawing at room temperature. To remove excess reagents, purification process by centrifugation at 14,000 rpm for 10 min was performed and the precipitation was re-suspended in water.

MnO_2 nanosheets were prepared by one-step process according to a previous report [45]. Typically, a mixed aqueous solution of tetramethylammonium hydroxide (0.6 M) and H_2O_2 (3 wt%) was prepared. 20

mL of the above solution was added to 10 mL of $MnCl_2$ (0.3 M) within 15 s. The blended solution turned to dark brown immediately, which was stirred overnight at room temperature. Afterwards, the as-prepared bulk MnO_2 nanosheets were centrifuged at 2000 rpm for 10 min, which were further washed with abundant distilled water and methanol, respectively. Afterwards, the nanosheets were dried at 60 °C 5 mg of MnO_2 was then dissolved in 10 mL of water and ultrasonicated for 10 h. Subsequently, the dispersion was centrifuged at 2000 rpm for 30 min and the supernatant was used in the following experiments.

2.3. $MnO_2@Au$ nanostructures with DNAzymes

50 μL of MnO_2 nanosheets (500 μg/mL) was blended with 50 μL of bare AuNPs, which was then treated with AA (5 mM) for 10 min before the measurements of UV–vis absorption spectra. To investigate the DNA protection effect, the mixture of MnO_2 and AuNPs were blended with DNA of a series of concentrations and lengths for 30 min at room temperature. Next, 5 mM AA treatments were performed. A mixture of Probe D and Probe S was prepared with the concentrations of 20 nM and 300 nM, respectively. It was then blended with 4 μL of MnO_2 nanosheets (500 μg/mL) before treated with 1 μL of AA (5 mM). The final volume of the solution was 50 μL and was kept at 4 °C for 4 h. Next, 50 μL of AuNPs and 150 μL of ultrapure water were added before measurements.

2.4. $MnO_2@Au$ nanostructures for miRNA assay amplified by HCR

Four single stranded strands (Probe H1, 2, 3, 4) with the concentrations of 10 nM were blended with Probe S1 (300 nM) and then target miRNA. DSN with the concentration of 3 U/mL was added for cleavage reaction at 56 °C. Afterwards, 4 μL of MnO_2 nanosheets (100 μg/mL) and 5 μL of AA (1 mM) were added into the above mixture. The final volume was kept to be 50 μL. HCR was carried out at room temperature for 4 h. Subsequently, 50 μL of AuNPs and 150 μL of pure water were further added before the measurements of UV–vis absorption spectra.

2.5. DNA-AuNPs protection of MnO_2 from salt induced aggregation

60 μL of DNA modified AuNPs was incubated with 30 μL of MnO_2 nanosheets (500 μg/mL) at room temperature for 30 min. Next, NaCl was added with different concentrations (0, 2.5, 5, 7.5, 10, 12.5, 15, 20, 25, 30, 40, 50 mM). The mixtures were heated to 56 °C for 2 min. After that, the solutions were centrifuged at 3050 rpm for 20 s. UV–vis absorption spectra were then recorded.

2.6. $MnO_2@Au$ nanostructures for miRNA assay amplified by CHA

Target miRNA with a series of concentrations (0.05, 0.5, 1, 1.5, 2, 2.5, 5, 10, 20, 30, 40, 50 nM) were blended with Probe H5, 6, 7 (45 nM) and H8 modified AuNPs. DSN with the concentration of 3 U/mL was then added for cleavage reaction at 56 °C. After 3 h, 30 μL of the solutions were blend with 30 μL of MnO_2 nanosheets and 137 μL of water, which were incubated at room temperature for 30 min. Next, 3 μL of NaCl (1 M) was added and the solutions were heated to 56 °C for 2 min. After that, the solutions were centrifuged at 3050 rpm for 20 s. Subsequently, the supernatants were monitored by the Synergy HT multifunction microplate reader.

3. Results and discussion

3.1. Working mechanism of $MnO_2@Au$ nanostructures based biosensing

MnO_2 nanosheets adsorb single-stranded DNA via the synergistic physisorption of nucleobases on the basal plane of nanosheets and co-ordination of phosphate [46]. We first investigate the nanosystem of DNA modified MnO_2 nanosheets and bare AuNPs. Probe D1, S1, D3, S3 are designed, in which Probe D1 and D3 act as Mn^{2+}-dependent DNAzymes,

while Probe S1 and S3 are corresponding substrates. Probe S1 contains only one cleavage site and can be divided from 12 nt single strand into two halves. Probe S3 contains three sites and the 24 nt strand can be divided into four parts. As shown in Scheme 1, the four strands are initially adsorbed on MnO_2 nanosheets. After the addition of AA, MnO_2 nanosheets are degraded. The generated Mn^{2+} and gradually released DNA strands from the nanosheets participate in the following DNAzyme catalyzed cleavage reactions. Long substrates are cleaved into short strands. Original long substrates can effectively protect AuNPs from salt-induced aggregation. However, the shortened strands lose the capabilities and AuNPs tend to aggregate in the presence of salt. This phenomenon is then applied as colorimetric output for miRNA assay. The recognition and signal transduction procedures are designed combining DSN and strand displacement-based hybridization chain reaction (HCR). Another four probes (Probe H1, 2, 3, 4) are introduced. The hairpin structures of these strands are kept stable at the DSN cleavage temperature of 56 °C (Fig. S1). Generally, target miRNA opens the hairpin of H1 and the duplex region is recognized by DSN. After digestion, miRNA is recycled for additional reactions. The remained single-stranded segment of H1 in turn opens the hairpin of H2, releasing another single-stranded segment, which triggers HCR with H3 and H4 as the fuel strands. Different from traditional HCR, the adjacent 5′ and 3′ terminals of H3 and H4 compose DNAzyme sequences along the primary chain and cleaves numerous Probe S1 strands. By evaluating the deprotecting efficiency of bare AuNPs from aggregation, initial miRNA levels can be determined. In this place, MnO_2 nanosheets and AuNPs are simply mixed together. AuNPs act as the colorimetric indicator, which respond to the DNA structure transition in the nanosystem.

We further explore the nanosystem of bare MnO_2 and DNA modified AuNPs, taking the aggregation of MnO_2 as the colorimetric output. As shown in Scheme 2, another four hairpin-structured oligonucleotides (Probe H5, H6, H7, H8) are designed, which are also stable at the DSN cleavage temperature of 56 °C (Fig. S2). miRNA opens hairpin of H5 by

hybridization reaction. The followed DSN catalyzed reaction recycles miRNA and generates abundant single-stranded part of H5 for successive CHA reactions. Briefly, hairpin structured H6 is opened and an intermediate is formed which is kept stable in DSN environment. The single-stranded part further interacts with H7 by forming double-stranded section. This section is long enough to be recognized by DSN. As a result, the released strand can be used to assist the digestion of H8 on AuNPs in a similar way. Initially, H8 modified AuNPs are conjugated with MnO_2 nanosheets. Due to the single-stranded region of DNA, salt induced aggregations of AuNPs and MnO_2 can be effectively inhibited. However, after target miRNA induced H8 degradation, AuNPs are no longer covered with DNA strands and the anti-aggregation capability is lost, leading to the changes of dispersion states of AuNPs and MnO_2 nanosheets. By analyzing the characteristic absorption of MnO_2, the concentration of miRNA trigger can be evaluated.

3.2. MnO_2 degradation induced AuNPs aggregation

Fig. 1A shows the TEM image of the mixture of MnO_2 nanosheets and AuNPs. Ultrathin lamellar morphology of MnO_2 nanosheets could be clearly observed and spherical AuNPs are well dispersed. UV–vis absorption spectra of MnO_2 and AuNPs with different ratios are compared in Fig. 1B. Inset is the picture of the MnO_2@Au nanostructures with different ratios. Two absorbance peaks at 350 nm and 520 nm are mainly ascribed to MnO_2 and AuNPs, respectively. From curve 1 to 6, the amounts of MnO_2 nanosheets are fixed and AuNPs levels are increased. Therefore, the absorbance at 520 nm (A_{520}) grows significantly and A_{350} also increases due to the absorbance of AuNPs at 350 nm. From curve 7 to 13, the concentrations of AuNP are the same while MnO_2 nanosheets levels are decreased. Therefore, A_{350} drops sharply and with slighted decreased A_{520}. The results indicate that the two peaks at 520 nm and 350 nm can be mainly ascribed to the two nanomaterials, which do not affect each other's UV–vis absorption performances significantly. Since
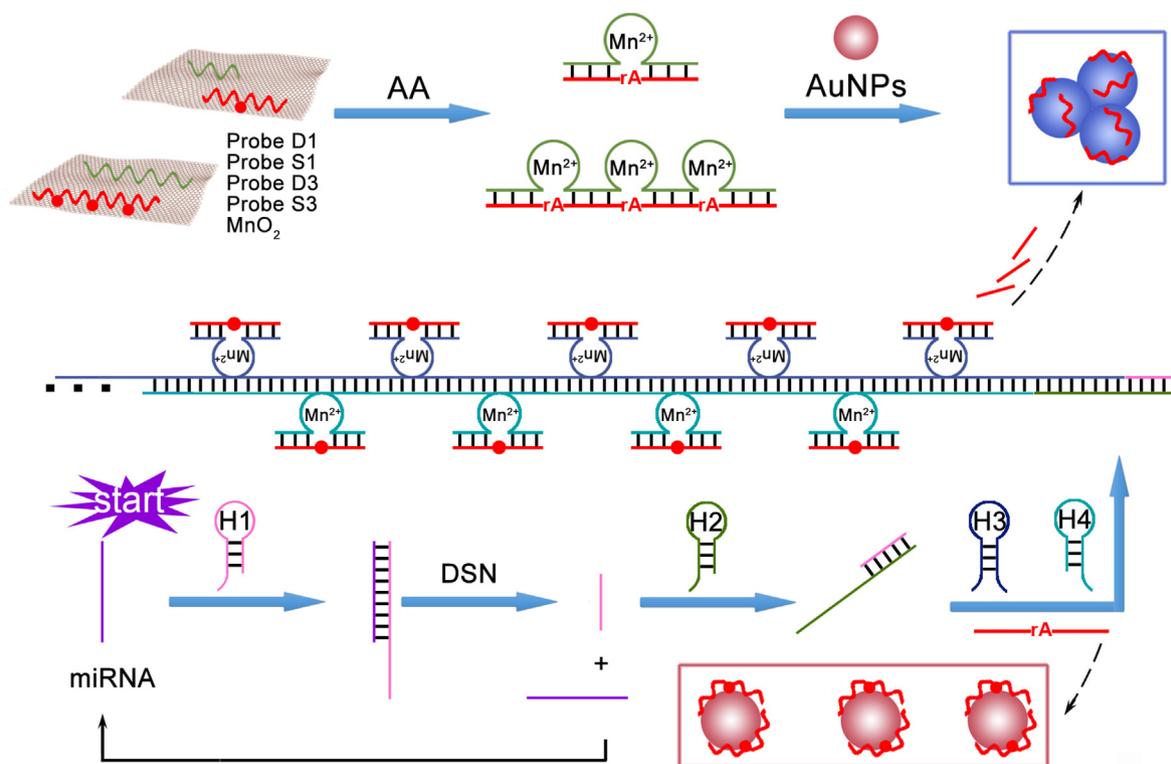
Scheme 1. Illustration of target triggered AuNPs aggregation with DSN-assisted HCR.
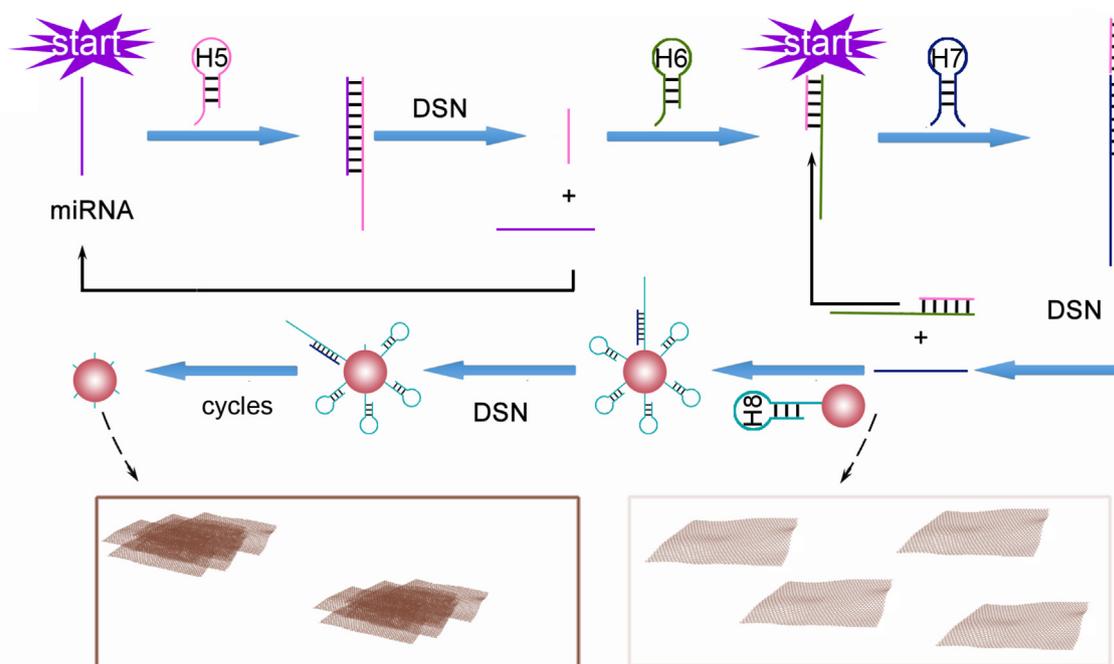
Scheme 2. Illustration of target triggered MnO_2 aggregation with DSN-assisted CHA.

both of AuNPs and MnO_2 undergoes aggregation with sufficient salt, different levels of NaCl are spiked in the MnO_2@Au nanosystem. The UV–vis absorption spectra are revealed in Fig. 1C. A_{350} represents the aggregation state of MnO_2 nanosheets, while the ratio of absorbances at 650 nm and 520 nm ($A_{650/520}$) reflects the aggregation state of AuNPs [47]. Initially, trace NaCl does not affect A_{350} and $A_{650/520}$. With larger concentration of NaCl, A_{350} decreases and $A_{650/520}$ increases, which is as expected. AA could effectively reduce MnO_2 and the produced Mn^{2+} could directly induce the aggregation of AuNPs. Therefore, after the addition of AA, the peak at 350 nm decreases, verifying the decline of MnO_2; meanwhile, the peak at 520 nm decreases and 650 peak intensity is significantly enlarged, which is the evidence of AuNPs aggregation (Fig. 1D).

Before AA triggered reaction, the added single-stranded DNA with certain lengths may inhibit the aggregation of AuNPs to a certain degree. Therefore, although MnO_2 is degraded with decreased A_{350}, the peak at 520 nm is well kept, demonstrating AuNPs are still well dispersed. Taken $A_{650/520}$ as the indicator, we come to the conclusion that larger amount of MnO_2 provides more Mn^{2+}, which leads to more intensive aggregation of AuNPs (Fig. 1E). On the contrary, larger concentrations of DNA tend to protect AuNPs better, which is reflected by the relatively smaller $A_{650/520}$ values (Fig. 1F). The length effect of DNA is then studied. It is observed that longer DNA shows better capability to maintain the high A_{520} and low A_{650} (Fig. 1G). We have further checked the indicator of $A_{650/520}$ with different concentrations of DNA. Similar trends are achieved and the variation of $A_{650/520}$ becomes much faster with larger amount of DNA. The concentration of DNA and the length of DNA are two key factors that influence the protection effect against salt-induced aggregation [27]. Thus, the combined parameter, the product of the two parameters (concentration of DNA and length of DNA), is then studied, which is termed as CL. As shown in Fig. 1H, $A_{650/520}$ values decrease sharply from 1 to 12 nt. With longer sequences, the values become stable. Thus, the length effect between 1 and 12 nt is more obvious and we choose 12 nt as a critical length for detailed studies. With CL from 500 to 3000 nt nM, $A_{650/520}$ values for 12 nt and 6 nt lengths decrease and the difference reaches the maximum at 1200 nt nM, which is quite significant (Fig. 1I).

This result is the foundation of our design of the substrate (Probe S1) of DNAzyme (Probe D1). The length of Probe S1 is 12 nt. After cleavage, 6 nt length products are generated, which show quite different protection capability.

3.3. DSN and HCR amplified biosensing

The first colorimetric biosensor is based on the MnO_2 degradation and subsequent AuNPs aggregation. It is clear that the salt treated AuNPs suffer significant changes of dispersion state (Fig. 2A and B). Bare AuNPs show uniform size centered around 13 nm. Although 12 nt is found to be the critical length, we have also designed a 24 nt length substrate (Probe S3) which can be divided into four segments after the cleavage of DNAzyme (Probe D3). The performances of Probe D1/S1 system and Probe D3/S3 system are directly compared in Fig. 2C. Detailed $A_{650/520}$ values are summarized in Fig. 2D, which are quite approaching to each other. The results further confirm the saturation state of DNA length for the protection of AuNPs from salt-induced aggregation. Therefore, we choose Probe S1 (12 nt) and Probe D1 in the following experiments.

The feasibility of this colorimetric biosensor is characterized by UV–vis absorption spectra and PAGE image. As shown in Fig. 3A, the curve of MnO_2@Au nanostructures after AA treatment shows a declined 520 nm peak and an emerging 650 nm peak. After protected by Probe S1, AuNPs possess better salt tolerance with nearly unchanged 520 nm peak compared with bare AuNPs. After the employment of miRNA and four hairpin strands, HCR occurs with numerous DNAzyme side chains. Therefore, Probe S1 strands are cleaved and with the shorter strands. The increase of $A_{650/520}$ indicates the poor protection efficiency. The assembly of HCR is also verified by PAGE characterization with expected bands (Fig. 3B). Generally, lane 1, 2, and 3 show the bands of miRNA, H1 and H2, respectively. Lane 4 shows two bands of H1 and H2, demonstrating that the blended two strands cannot interact with each other directly. Lane 5 is the products of miRNA, H1 and H2 in the presence of DSN. The new bands are ascribed to H1/miRNA and H1/2 duplexes, respectively. Lane 6 shows the band of H3 and H4. Due to the same length of H3 and H4, only one band is observed. After directly mixing H1, H2,
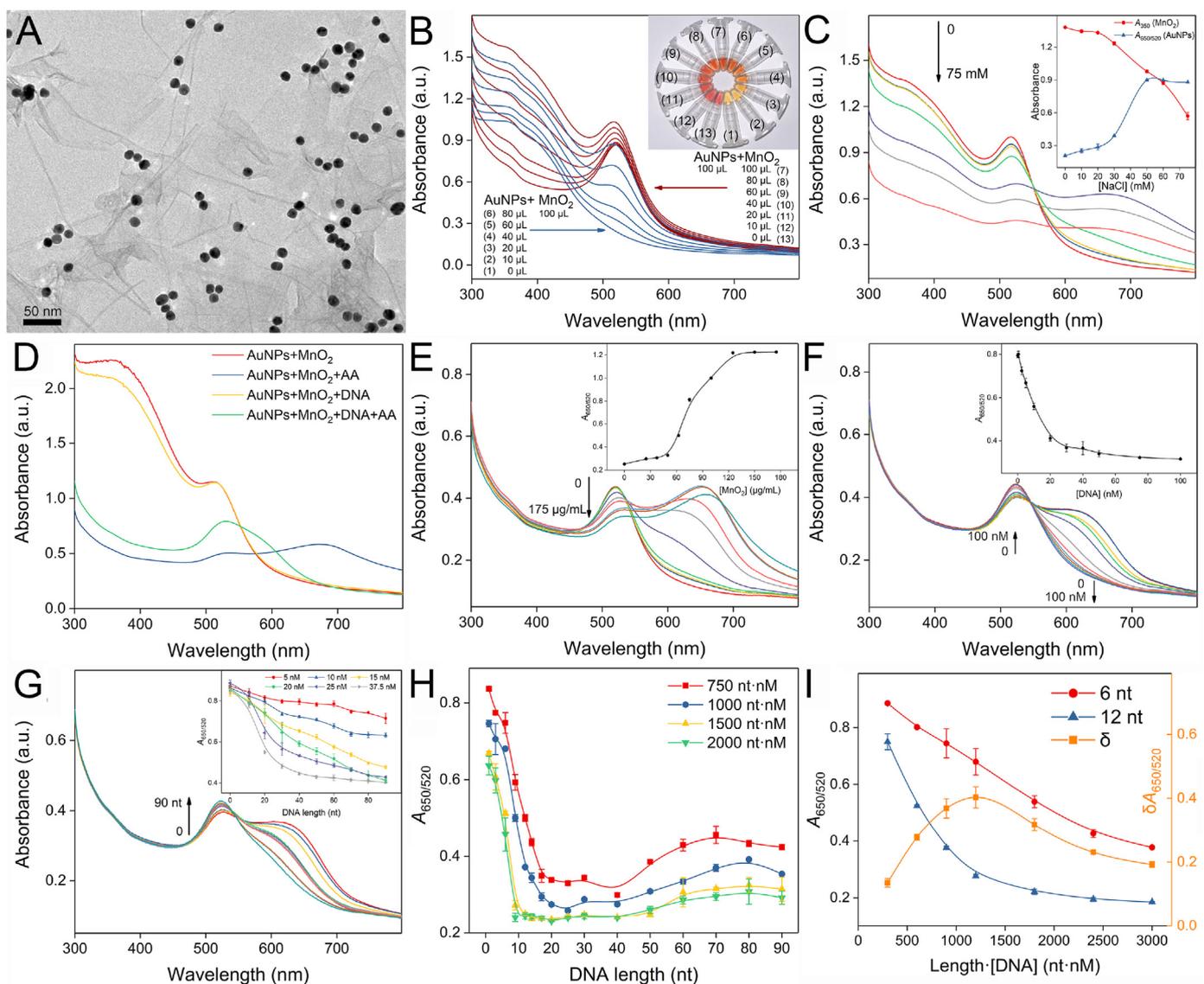
Fig. 1. (A) TEM image of MnO_2@AuNPs. (B) UV–vis spectra of DNA (100 nM) protected mixtures of MnO_2 and AuNPs after treated with 10 nM NaCl. Inset is the picture. (C) UV–vis spectra of MnO_2@AuNPs after treated with NaCl. Inset shows the relationships between NaCl concentration and A_{350} or $A_{650/520}$. (D) UV–vis spectra of MnO_2@AuNPs with and without protection of DNA after treated with 5 mM AA. (E) UV–vis spectra of MnO_2@AuNPs of different concentrations after treated with 5 mM AA. Inset shows the relationship between $A_{650/520}$ versus MnO_2 concentration. (F) UV–vis spectra of MnO_2@AuNPs protected by DNA after treated with salt. Inset shows the relationship between $A_{650/520}$ versus DNA concentration (30 nt). (G) UV–vis spectra of MnO_2@AuNPs protected by 20 nM DNA with different lengths. Inset shows $A_{650/520}$ versus DNA length. (H) Relationship between $A_{650/520}$ and DNA length with unique CL values. (I) Relationship between $A_{650/520}$ and CL with DNA sizes of 6 nt and 12 nt.

H3, and H4, the corresponding bands of the DNA probes are shown in lane 7, verifying that the four stands cannot form HCR product directly. However, after the introduction of miRNA and DSN, hairpin opening reaction and digestion cycles help the HCR assembly and the bands with larger molecules weights are ascribed to the HCR products.

Before quantitative analysis of target triggered DNA structure transition, some important parameters are optimized including 20 nM Probe D1, 300 nM Probe S1, 20 μM AA, and 8 μg/mL MnO_2 (Fig. S3). The reduction reaction of MnO_2 is demonstrated to be quite fast (Fig. S4). Under these conditions, standard miRNA samples with a series of concentrations are prepared to trigger DNA structural transitions with DSN cleavage. The UV–vis absorption spectra are recorded and shown in Fig. 3C. With the increase of miRNA from 0 to 20 nM, the peak at 520 nm decreases and the peak at 650 nm increases. Detailed relationship

between $A_{650/520}$ and the concentration of miRNA is depicted in Fig. 3D. The linear range is from 0.5 to 12.5 nM with the equation as follows:

$$y = 0.535 + 0.00756\,x\ (n = 3, R^2 = 0.996)$$

in which y is $A_{650/520}$ and x is the concentration of miRNA. The limit of detection of this colorimetric assay is evaluated to be 100 pM (S/N = 3). We have also checked the anti-interfering ability of this biosensor. Since DSN is able to discriminate perfectly matched duplexes and mismatched duplexes even with one mismatched site [48], the selectivity is excellent, which is demonstrated by the comparison of $A_{650/520}$ values for target miRNA and mismatched sequences (Fig. 3E). Besides, this colorimetric biosensor performs well in biological circumstances with approaching values with those in PBS conditions (Fig. 3F).
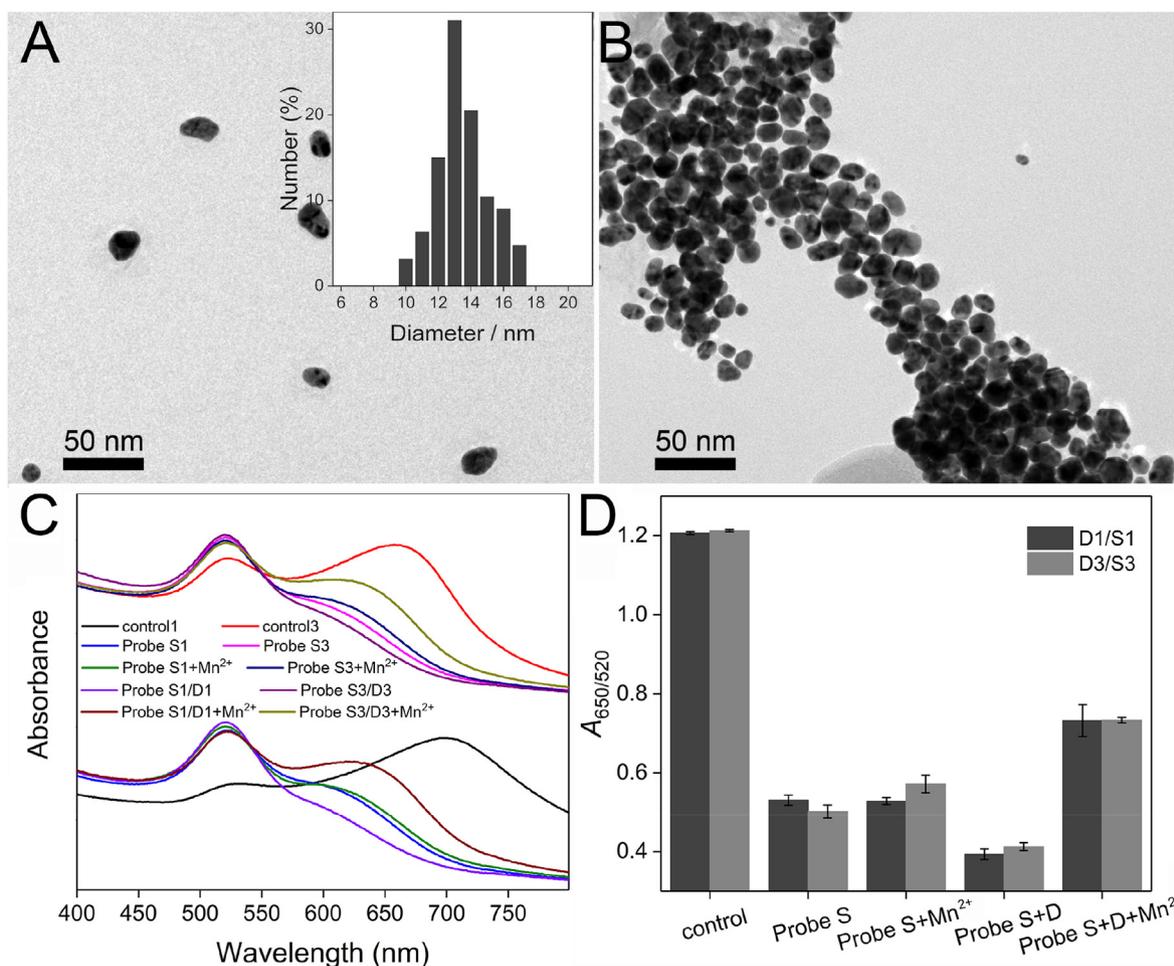
Fig. 2. TEM images of AuNPs (A) before and (B) after treated with salt. (C) UV–vis spectra of AuNPs without and with the additions of Probe S, Probe D, Probe S/D and then the treatment of Mn^{2+}. (D) Histogram of calculated $A_{650/520}$ values.

3.4. MnO₂ aggregation based colorimetric biosensing amplified by DSN and CHA

The second colorimetric biosensor is based on target triggered DNA degradation on AuNPs, which induced aggregation of MnO_2 nanosheets. From UV–vis absorption spectra in Fig. 4A, it is clear that bare MnO_2 and AuNPs cannot resist salt-induced aggregation. Both of the peaks at 350 nm and 650 nm disappear. On the contrary, the mixture of H8 modified AuNPs and MnO_2 shows high peak intensities at 350 nm and 520 nm, which is ascribed to the protection of DNA strands to increase the salt tolerance of the nanosystem. However, after the introduction of miRNA, catalytic hairpin assembly (CHA) and DSN cleavage reaction are performed to digest H8 [49]. As a result, the peak at 350 nm drops significantly, indicating that colloidal MnO_2 is quite sensitive to salt and is suitable to be used as colorimetric output. The DNA assembly and digestion reactions are confirmed by PAGE image, in which CHA and digested products are positioned at expected sites (Fig. 4B).

Next, we have optimized several critical parameters for colorimetric biosensing by comparing the index of A_{350} in the absence and presence of target miRNA. For example, larger amount of DNA modified AuNPs are supposed to protect MnO_2 better; salt with extremely low or much high concentrations might result in limited colorimetric differences due to the well-dispersed or highly aggregated states; the DSN concentration, reaction time and temperature might also affect the digestion degree. After comparing the A_{350} values, optimal amount of AuNPs, concentrations of salt, DSN, reaction time and temperature are selected to be 60 μL, 15 mM, 3 U/mL, 2 min and 56 °C, respectively (Fig. S5). Upon these conditions, a

series of concentrations of miRNA are spiked in the $MnO_2@Au$ nanostructures and corresponding UV–vis adsorption spectra are measured. Larger amount of miRNA leads to more intensive aggregation of MnO_2, which can be reflected by the gradually decreased peak at 350 nm (Fig. 4C). The color of solutions turns from yellow to transparent, which can be observed by naked eyes. The aggregated state of MnO_2 nanosheets are also confirmed by the TEM image (Fig. S6). Detailed relationship between A_{350} and miRNA concentrations is established in Fig. 4D. The linear range is from 0.05 to 5 nM. The equation is as follows:

$$y = 0.979 – 0.138\,x\ (n = 3,\ R^2 = 0.960)$$

in which y is A_{350} and x is the concentration of miRNA. The limit of detection of this colorimetric biosensor is calculated as 10 pM (S/N = 3), which is satisfactory and show superiority compared with recently reported methods (Table S2). The limit of detection is lower than the above-mentioned HCR-assisted colorimetric system. The high sensitivity is owing to the integration of DSN catalyzed reaction and highly efficient CHA cycles. Moreover, the operation of this biosensor is quite facile by taking good use of the features of $MnO_2@Au$ nanostructures. We have also employed mismatched sequences to check the selectivity of this approach. Only target miRNA can lead to the aggregation of MnO_2 with significantly declined A_{350}, which is in good accordance with the above colorimetric biosensor (Fig. 4E). The spiked miRNA in clinical serums samples can be successfully distinguished with nearly the same optical responses as in PBS conditions, demonstrating good practical utility (Fig. 4F).
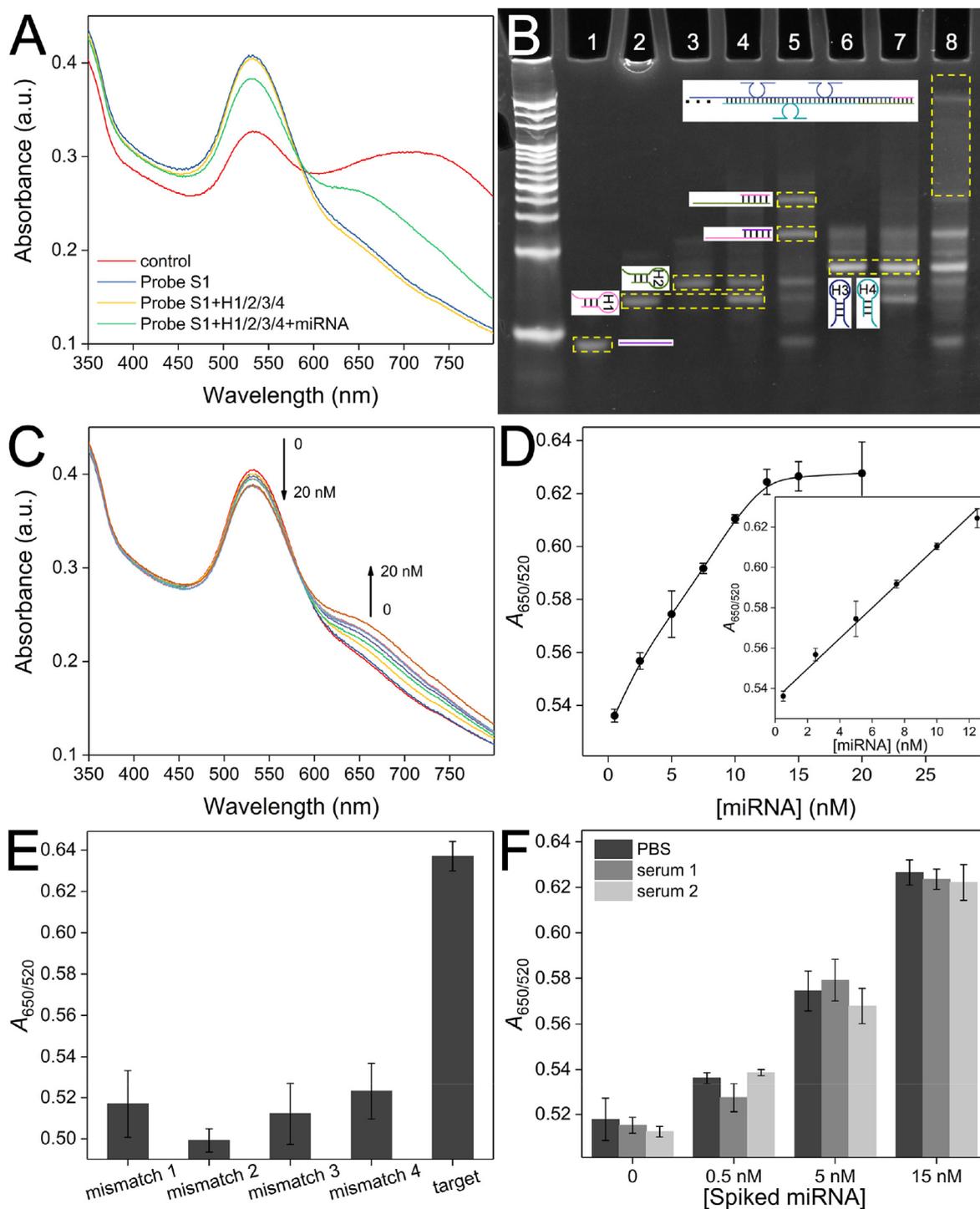
Fig. 3. (A) UV–vis spectra of AA treated MnO$_2$@AuNPs without and with protection of Probe S1 (before and after HCR product cleavage). miRNA: 25 nM; Probe S1: 300 nM. (B) PAGE analysis of DNA structural transitions: (1) miRNA, (2) H1, (3) H2, (4) H1 and H2, (5) miRNA, H1 and H2, (6) H3 and H4, (7) H1, H2, H3 and H4, (8) miRNA, H1, H2, H3 and H4. (C) UV–vis spectra for the detection of miRNA with the concentrations of 0, 0.5, 2.5, 5, 7.5, 10, 12.5, 15, 20 nM. (D) Calibration curve representing the relationship between A$_{650/520}$ and miRNA concentration. Inset shows the linear range. (E) A$_{650/520}$ values for the analysis of target miRNA and mismatched sequences. (F) Comparison of analytical performances in PBS and human serum samples.

4. Conclusions

In summary, we systematically investigate the aggregation and dispersion mechanism of MnO$_2$@Au nanosystem. MnO$_2$ degradation not only provides salt environment but also assist the function of DNAzyme, which acts on aggregation of AuNPs. In addition, the variation of DNA strands on AuNPs can also influence the dispersion state of MnO$_2$ in the absence of reductants. Two colorimetric biosensing strategies with the aggregations of AuNPs or MnO$_2$ are then developed, respectively. DSN catalyzed reaction and target miRNA induced DNA structural transition are applied for signal amplification. The biosensors demonstrate high sensitivity with the LOD of 10 pM under optimal conditions. Moreover, excellent selectivity and anti-interference ability are displayed after challenging mismatched sequences and clinical samples. Therefore, this
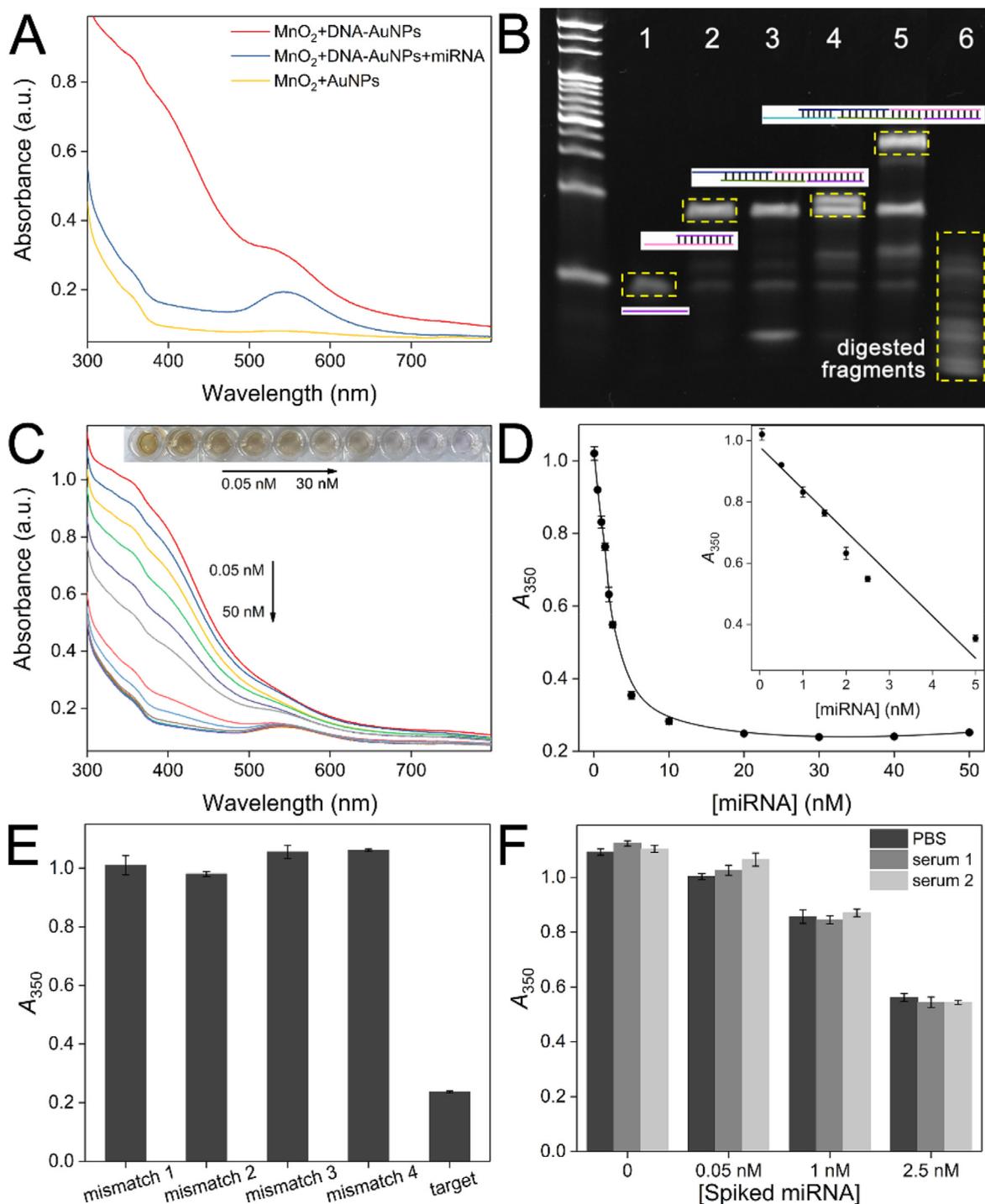
Fig. 4. (A) UV–vis spectra of 15 mM NaCl treated MnO_2 nanosheets with AuNPs, DNA-AuNPs in the presence and absence of miRNA triggered reactions. (B) PAGE analysis of CHA process: (1) miRNA, (2) miRNA and H5, (3) miRNA, H5 and H6, (4) miRNA, H5, H6 and H7, (5) miRNA, H5, H6, H7 and H8, (6) miRNA, H5, H6, H7, H8 and DSN. (C) UV–vis spectra for the detection of miRNA with the concentrations of 0.05, 0.5, 1, 1.5, 2, 2.5, 5, 10, 20, 30, 40, 50 nM. (D) Calibration curve representing the relationship between A_{350} and miRNA concentration. Inset shows the linear range. (E) A_{350} values for the analysis of target miRNA and mismatched sequences. (F) Comparison of analytical performances in PBS and human serum samples.

work offers powerful tools for quantitative analysis of miRNA on the basis of the attractive features of MnO_2@Au nanostructures, which has great potential utility. In this study, the colorimetric responses are from either the aggregation states of AuNPs or MnO_2 nanosheets. Since these nanomaterials also exhibit certain nanozyme activities, more possibilities of colorimetric outputs might be explored by introducing more substrates, which deserve further investigations.

Credit author statement

Xiaoyi Ma: Methodology, Investigation, Writing – Original Draft. Wuping Zhou: Data Curation, Formal Analysis. Haiwen Li: Formal Analysis, Methodology. Bo Zhang: Validation, Writing- Review & Editing. Peng Miao: Conceptualization, Writing- Review & Editing, Project Administration.

Declaration of competing interest

The authors declare that they have no known competing financial interests or personal relationships that could have appeared to influence the work reported in this paper.

Data availability

Data will be made available on request.

Acknowledgments

Appendix A. Supplementary data

Supplementary data to this article can be found online at https://doi.org/10.1016/j.mtbio.2023.100571.

References

[1] P. Gao, P. Metz, T. Hey, Y.X. Gong, D.W. Liu, D.D. Edwards, J.Y. Howe, R. Huang, S.T. Misture, The critical role of point defects in improving the specific capacitance of δ-MnO2 nanosheets, Nat. Commun. 8 (2017), 14559.

[2] G.B. Yang, L.G. Xu, Y. Chao, J. Xu, X.Q. Sun, Y.F. Wu, R. Peng, Z. Liu, Hollow MnO2 as a tumor-microenvironment-responsive biodegradable nano-platform for combination therapy favoring antitumor immune responses, Nat. Commun. 8 (2017) 902.

[3] L.T. Yang, S.-T.D. Chueng, Y. Li, M. Patel, C. Rathnam, G. Dey, L. Wang, L. Cai, K.-B. Lee, A biodegradable hybrid inorganic nanoscaffold for advanced stem cell therapy, Nat. Commun. 9 (2018) 3147.

[4] Z.H. Huang, Y. Song, D.Y. Feng, Z. Sun, X.Q. Sun, X.X. Liu, High mass loading MnO2 with hierarchical nanostructures for supercapacitors, ACS Nano 12 (2018) 3557–3567.

[5] S.P. Rong, P.Y. Zhang, Y.J. Yang, L. Zhu, J.L. Wang, F. Liu, MnO2 framework for instantaneous mineralization of carcinogenic airborne formaldehyde at room temperature, ACS Catal. 7 (2017) 1057–1067.

[6] P.F. Xia, B.C. Zhu, B. Cheng, J.G. Yu, J.S. Xu, 2D/2D g-C3N4/MnO2 nanocomposite as a direct Z-scheme photocatalyst for enhanced photocatalytic activity, ACS Sustain. Chem. Eng. 6 (2018) 965–973.

[7] Q. Chen, L.Z. Feng, J.J. Liu, W.W. Zhu, Z.L. Dong, Y.F. Wu, Z. Liu, Intelligent albumin–MnO2 nanoparticles as pH-/H2O2-responsive dissociable nanocarriers to modulate tumor hypoxia for effective combination therapy, Adv. Mater. 28 (2016) 7129–7136.

[8] X. Guan, L.P. Sun, Y.T. Shen, F.S. Jin, X.W. Bo, C.Y. Zhu, X.X. Han, X.L. Li, Y. Chen, H.X. Xu, W.W. Yue, Nanoparticle-enhanced radiotherapy synergizes with PD-L1 blockade to limit post-surgical cancer recurrence and metastasis, Nat. Commun. 13 (2022) 2834.

[9] Z.J. Shen, Q.M. Ma, X.Y. Zhou, G.M. Zhang, G.Z. Hao, Y. Sun, J. Cao, Strategies to improve photodynamic therapy efficacy by relieving the tumor hypoxia environment, NPG Asia Mater. 13 (2021) 39.

[10] L. Wang, S.Y. Guan, Y.Z.W. Weng, S.M. Xu, H. Lu, X.M. Meng, S.Y. Zhou, Highly efficient vacancy-driven photothermal therapy mediated by ultrathin MnO2 nanosheets, ACS Appl. Mater. Interfaces 11 (2019) 6267–6275.

[11] X.H. Zhu, R. Tang, S.G. Wang, X.Y. Chen, J.J. Hu, C.Y. Lei, Y. Huang, H.H. Wang, Z. Nie, S.Z. Yao, Protein@inorganic nanodumpling system for high-loading protein delivery with activatable fluorescence and magnetic resonance bimodal imaging capabilities, ACS Nano 14 (2020) 2172–2182.

[12] J. Liu, L.J. Meng, Z.F. Fei, P.J. Dyson, X.N. Jing, X. Liu, MnO2 nanosheets as an artificial enzyme to mimic oxidase for rapid and sensitive detection of glutathione, Biosens. Bioelectron. 90 (2017) 69–74.

[13] J.H. Wu, Q.T. Yang, Q. Li, H.Y. Li, F. Li, Two-dimensional MnO2 nanozyme-mediated homogeneous electrochemical detection of organophosphate pesticides without the interference of H2O2 and color, Anal. Chem. 93 (2021) 4084–4091.

[14] Y.Z. Yao, P. Li, J.K. He, D.D. Wang, J. Hu, X.L. Yang, Albumin-templated Bi2Se3–MnO2 nanocomposites with promoted catalase-like activity for enhanced radiotherapy of cancer, ACS Appl. Mater. Interfaces 13 (2021) 28650–28661.

[15] G.X. Zhu, W. Zhu, Y. Lou, J. Ma, W.Q. Yao, R.L. Zong, Y.F. Zhu, Encapsulate α-MnO2 nanofiber within graphene layer to tune surface electronic structure for efficient ozone decomposition, Nat. Commun. 12 (2021) 4152.

[16] Z.L. Zhao, H.H. Fan, G.F. Zhou, H.R. Bai, H. Liang, R.W. Wang, X.B. Zhang, W.H. Tan, Activatable fluorescence/MRI bimodal platform for tumor cell imaging via MnO2 nanosheet–aptamer nanoprobe, J. Am. Chem. Soc. 136 (2014) 11220–11223.

[17] T. Song, Y. Liao, Q.H. Zuo, N. Liu, Z.H. Liu, MnO2 nanoparticles as a minimalist multimode vaccine adjuvant/delivery system to regulate antigen presenting cells for tumor immunotherapy, J. Mater. Chem. B 10 (2022) 3474–3490.

[18] S.K. Chondath, A.P.K. Sreekala, C. Farzeena, S.N. Varanakkottu, M.M. Menamparambath, Interfacial tension driven adsorption of MnO2 nanoparticles at the liquid/liquid interface to tailor ultra-thin polypyrrole sheets, Nanoscale 14 (2022) 11197–11209.

[19] J.Q. Dong, K. Zhang, X. Li, Y.H. Qian, H. Zhu, D.Q. Yuan, Q.H. Xu, J.W. Jiang, D. Zhao, Ultrathin two-dimensional porous organic nanosheets with molecular rotors for chemical sensing, Nat. Commun. 8 (2017) 1142.

[20] W. Luc, X.B. Fu, J.J. Shi, J.J. Lv, M. Jouny, B.H. Ko, Y.B. Xu, Q. Tu, X.B. Hu, J.S. Wu, Q. Yue, Y.Y. Liu, F. Jiao, Y.J. Kang, Two-dimensional copper nanosheets for electrochemical reduction of carbon monoxide to acetate, Nat. Catal. 2 (2019) 423–430.

[21] G.H. Yang, C.Z. Zhu, D. Du, J.J. Zhu, Y.H. Lin, Graphene-like two-dimensional layered nanomaterials: applications in biosensors and nanomedicine, Nanoscale 7 (2015) 14217–14231.

[22] R. Ma, Y. Bando, L. Zhang, T. Sasaki, Layered MnO2 nanobelts: hydrothermal synthesis and electrochemical measurements, Adv. Mater. 16 (2004) 918–922.

[23] J.X. Xie, H.Y. Cao, H. Jiang, Y.J. Chen, W.B. Shi, H.Z. Zheng, Y.M. Huang, Co3O4-reduced graphene oxide nanocomposite as an effective peroxidase mimetic and its application in visual biosensing of glucose, Anal. Chim. Acta 796 (2013) 92–100.

[24] W.Y. Zhai, C.X. Wang, P. Yu, Y.X. Wang, L.Q. Mao, Single-layer MnO2 nanosheets suppressed fluorescence of 7-hydroxycoumarin: mechanistic study and application for sensitive sensing of ascorbic acid in vivo, Anal. Chem. 86 (2014) 12206–12213.

[25] C.P. Liang, J.L. Chen, M.Q. Li, Z.L. Ge, C.H. Fan, J.L. Shen, Probing the self-assembly process of amphiphilic tetrahedral DNA frameworks, Chem. Commun. 58 (2022) 8352–8355.

[26] X.G. Liu, F. Zhang, X.X. Jing, M.C. Pan, P. Liu, W. Li, B.W. Zhu, J. Li, H. Chen, L.H. Wang, J.P. Lin, Y. Liu, D.Y. Zhao, H. Yan, C.H. Fan, Complex silica composite nanomaterials templated with DNA origami, Nature 559 (2018) 593–598.

[27] H. Chai, X.Y. Ma, H.X. Sun, P. Miao, DNA–MnO2 nanoconjugates investigation and application for electrochemical polymerase chain reaction, Anal. Chem. 94 (2022) 4565–4569.

[28] W.P. Fan, W.B. Bu, B. Shen, Q.J. He, Z.W. Cui, Y.Y. Liu, X.P. Zheng, K.L. Zhao, J.L. Shi, Intelligent MnO2 nanosheets anchored with upconversion nanoprobes for concurrent pH-/H2O2-responsive UCL imaging and oxygen-elevated synergetic therapy, Adv. Mater. 27 (2015) 4155–4161.

[29] R.R. Deng, X.J. Xie, M. Vendrell, Y.T. Chang, X.G. Liu, Intracellular glutathione detection using MnO2-nanosheet-modified upconversion nanoparticles, J. Am. Chem. Soc. 133 (2011) 20168–20171.

[30] Q.Q. Shi, S.Y. Pu, X. Yang, P. Wang, B. Tang, B. Lai, Enhanced heterogeneous activation of peroxymonosulfate by boosting internal electron transfer in a bimetallic Fe3O4-MnO2 nanocomposite, Chin. Chem. Lett. 33 (2022) 2129–2133.

[31] S. Murke, K. Wonner, S.R. Alfarano, C. Rurainsky, P. Cignoni, K. Tschulik, M. Havenith, SERS reveals the presence of Au–O–O–H and enhanced catalytic activity of electrochemically dealloyed AgAu nanoparticles, J. Phys. Chem. C 127 (2023) 1071–1076.

[32] D. Li, X.L. Zhang, Y.Q. Chai, R. Yuan, Controllable three-dimensional DNA nanomachine-mediated electrochemical biosensing platform for rapid and ultrasensitive detection of microRNA, Anal. Chem. 95 (2023) 1490–1497.

[33] S. Fazal, A. Jayasree, S. Sasidharan, M. Koyakutty, S.V. Nair, D. Menon, Green synthesis of anisotropic gold nanoparticles for photothermal therapy of cancer, ACS Appl. Mater. Interfaces 6 (2014) 8080–8089.

[34] M. Cárdenas, J. Barauskas, K. Schillén, J.L. Brennan, M. Brust, T. Nylander, Thiol-specific and nonspecific interactions between DNA and gold nanoparticles, Langmuir 22 (2006) 3294–3299.

[35] Y. Song, M.Y. Wang, Q. Qian, J. Xu, Q.G. Zhou, S.J. Lv, P. Miao, Trace miRNA Assay based on DNA nanostructures formed by hybridization chain reaction and gold-nanoparticle tags, Chemelectrochem 8 (2021) 2778–2782.

[36] X. Zhang, M.R. Servos, J.W. Liu, Instantaneous and quantitative functionalization of gold nanoparticles with thiolated DNA using a pH-assisted and surfactant-free route, J. Am. Chem. Soc. 134 (2012) 7266–7269.

[37] B.W. Liu, J.W. Liu, Freezing directed construction of bio/nano interfaces: reagentless conjugation, denser spherical nucleic acids, and better nanoflares, J. Am. Chem. Soc. 139 (2017) 9471–9474.

[38] L. Chen, Y. Sun, M. Tang, D.L. Wu, Z.D. Xiang, C.P. Huang, B. You, D.D. Xie, Q.L. Ye, D.X. Yu, C.S. Chang, High-dose-androgen-induced autophagic cell death to suppress the Enzalutamide-resistant prostate cancer growth via altering the circRNA-BCL2/miRNA-198/AMBRA1 signaling, Cell Death Discovery 8 (2022) 128.

[39] C. Zhang, Y.M. Zhao, X.M. Xu, R. Xu, H.W. Li, X.Y. Teng, Y.Z. Du, Y.Y. Miao, H.C. Lin, D. Han, Cancer diagnosis with DNA molecular computation, Nat. Nanotechnol. 15 (2020) 709–715.

[40] L. Hu, A.S. Stasheuski, D.W. Wegman, N. Wu, B.B. Yang, H. Hayder, C. Peng, S.K. Liu, G.M. Yousef, S.N. Krylov, Accurate microRNA analysis in crude cell lysate by capillary electrophoresis-based hybridization assay in comparison with quantitative reverse transcription-polymerase chain reaction, Anal. Chem. 89 (2017) 4743–4748.

[41] W.J. Brittain, T. Brandsetter, O. Prucker, J. Rühe, The surface science of microarray generation–a critical inventory, ACS Appl. Mater. Interfaces 11 (2019) 39397–39409.

[42] H. Chai, P. Miao, Ultrasensitive assay of ctDNA based on DNA triangular prism and three-way junction nanostructures, Chin. Chem. Lett. 32 (2021) 783–786.

[43] J. Jiao, C. Li, L. Ning, L. Shi, L. Wang, Y. Xiang, G.X. Li, Electrochemical detection of circRNAs based on the combination of back-splice junction and duplex-specific nuclease, Sens. Actuator B-Chem. 302 (2020), 127166.

[44] B. Bo, T. Zhang, Y.T. Jiang, H.Y. Cui, P. Miao, Triple signal amplification strategy for ultrasensitive determination of miRNA based on duplex specific nuclease and bridge DNA-gold nanoparticles, Anal. Chem. 90 (2018) 2395–2400.

[45] P. Miao, Y.G. Tang, Two-dimensional hybridization chain reaction strategy for highly sensitive analysis of intracellular mRNA, Anal. Chem. 92 (2020) 12700–12709.

[46] L. Wang, Z.C. Huang, Y.B. Liu, J. Wu, J.W. Liu, Fluorescent DNA probing nanoscale MnO2: adsorption, dissolution by thiol, and nanozyme activity, Langmuir 34 (2018) 3094–3101.

[47] R. Lévy, N.T.K. Thanh, R.C. Doty, I. Hussain, R.J. Nichols, D.J. Schiffrin, M. Brust, D.G. Fernig, Rational and combinatorial design of peptide capping ligands for gold nanoparticles, J. Am. Chem. Soc. 126 (2004) 10076–10084.

[48] S. Yu, Y.Y. Wang, L.P. Jiang, S. Bi, J.J. Zhu, Cascade amplification-mediated in situ hot-spot assembly for microRNA detection and molecular logic gate operations, Anal. Chem. 90 (2018) 4544–4551.

[49] X.H. Mao, Q. Li, X.L. Zuo, C.H. Fan, Catalytic nucleic acids for bioanalysis, ACS Appl. Bio Mater. 3 (2020) 2674–2685.